Hindawi
Advances in Materials Science and Engineering
Volume 2022, Article ID 9880484, 11 pages
https://doi.org/10.1155/2022/9880484

Research Article

High-Temperature Creep Behavior of a Nickel-Based Single-Crystal Superalloy with Small-Angle Deviation from [111] Orientation

Guangyan Wang,[1,2] Song Zhang ,[1] Guoqi Zhao,[2] Ning Tian,[2] Huajin Yan,[2] Sugui Tian,[1] and Fangwei Jin[2]

[1]*School of Materials Science and Engineering, Shenyang University of Technology, Shenyang 110870, China*
[2]*Guizhou Laboratory of Reliability Evaluation of Metal Material Under Specific Environment, Guizhou University of Engineering Science, Bijie 551700, China*

Correspondence should be addressed to Song Zhang; songzhang_sy@163.com

Received 15 August 2022; Accepted 27 October 2022; Published 7 November 2022

Academic Editor: Sonar Tushar

By means of tensile creep tests and microstructure analysis, the creep behavior and deformation mechanism of a nickel-based single-crystal alloy with small-angle deviations from the [111] orientation at 1040°C/137 MPa were investigated. The results suggested that in the early stage of creep, proliferating dislocations generated by different slip systems get accumulated in the γ phase. Dislocations mainly slipped in the γ phase and climbed over the γ' phase, and they began to form a dislocation network at the interface. γ' phases were connected to each other, and the coherence relationship was destroyed. In the steady-state stage of creep, the solid interfacial dislocation network was formed, and the γ' phase transformed into a lamellar raft structure, which hinders the slip and climb of dislocations in the matrix channel. In the accelerated creep stage, the dislocation network was destroyed, and dislocations sheared into the γ' phase in the way of dislocation pairs, which could react to form a superdislocation node and decompose to form APBs on the <111> plane or cross slip from the <111> plane to the <100> plane to form K-W locks.

1. Introduction

Nickel-based single-crystal alloys have become the key material for manufacturing advanced aeroengine blades and other hot-end parts owing to their excellent high-temperature mechanical properties and creep resistance [1–3]. The preferred growth direction of nickel-based single-crystal alloys is [001], and single-crystal alloys with the [001] orientation have excellent comprehensive performances at high temperatures [4]. Thus, the axial direction of single-crystal blades in industrial production is the [001] orientation. By ensuring that the [001] orientation of the minimum elastic modulus is consistent with the direction of the maximum load, the thermal cycling stress is reduced. However, in practice, single crystals with a preferred orientation deviate significantly from the loading direction, and a nonpreferred growth orientation is often obtained. In addition, blade parts themselves have complex geometric structures, such as intricate cooling channels, which cause the direction of centrifugal force actually borne by blade parts during operation to deviate from the [001] orientation, sometimes by very large amounts. Therefore, the problem of anisotropy should be fully considered when designing and manufacturing single-crystal blades.

The inherent crystallographic properties of nickel-based single-crystal alloys determine the anisotropy of their mechanical properties. The deviation between the load direction and crystal orientation is an important factor affecting the service life, and the main failure mode of nickel-based single-crystal alloys under high-temperature service conditions is creep damage. Therefore, the anisotropy of the creep behavior of nickel-based single-crystal alloys and the

creep mechanism of small-angle-deviated [001]-oriented alloys have been widely focused and studied by material researchers. When Mackay and Maier [5] studied the creep anisotropy of the Mar-M247 single-crystal superalloy with an [001] orientation deviation of less than 25° at 774°C/724 MPa, they found that compared with the alloy with an orientation close to the <001>-<$\bar{1}$11> boundary, the alloy whose crystal orientation was close to the <001>-<011> boundary had a better creep strength, which was consistent with Leverant and Kear's results for Mar-M200 alloys with orientations less than 18° from the [001] orientation [6]. The difference between MAR-M200 and MAR-M247 alloys is that the Mar-M247 alloy has the longest creep life near the <111> orientation, whereas the Mar-M200 alloy has the longest creep life when the orientation is close to <001>. Furthermore, for these alloys [7], creep lives of alloys did not show a significant decrease when the crystal orientation deviated from the <001> orientation by less than 20°. Among the samples with orientations of [001], [011], and [111], the creep life of the [111] orientation was the longest and that of the [011] orientation was the shortest. The study [8–10] by Rae et al. on the CMSX-4 alloy also showed that in the temperature range of 750–850°C, within the deviation range of 20° from the [001] orientation, the initial creep stage strongly depended on the degree of deviation of the alloy from the [001]-[011] edge. The alloy with an orientation close to the [001]-[011] edge had a lower initial creep strain and longer creep life because it was not easy to form a <112> dislocation [11]. However, alloys with orientations close to the [001]–[111] edge showed larger initial creep strains and shorter creep lives due to a large number of <112> dislocations cutting the γ' phase. The study [12] by Sass on the CMSX-4 alloy showed that the anisotropy of the creep strength was significant at 850°C and that the creep strength decreased successively in the orientation order of [001], [011], and [111], while the raft transformation of the γ' phase occurred at 980°C, and the anisotropy difference of the alloy decreased [13]. In addition, it was found in another study [14] that the inhomogeneity of plastic deformation decreased in the order of [011], [001], and [111]. The creep properties and microstructure of a nickel-based single-crystal superalloy DD413 with a 15° deviation from the <001> orientation were investigated at 760°C/793 MPa. The results [7] showed that the alloy with an orientation close to the <001>-<101> boundary had the longest creep life, and the creep life of the alloy orienting near the <001>-<111> boundary was the shortest [15]. The deformation of samples orienting near the <001>-<101> boundary was mainly controlled by the {111}<110> slip system, while the deformation of samples orienting near the <001>-<111> boundary was mainly controlled by the {111}<112> slip system [16].

Based on the above discussion, nickel-based single-crystal alloys with different orientations and deviations from the [001] orientation have been extensively studied, but there are few reports on nickel-based single-crystal alloys with small-angle deviations from the [111] orientation. In this study, a test bar of a nickel-based single-crystal alloy deviating from the [111] orientation by a certain angle was prepared, and creep properties were tested at high temperature. The microstructural morphology of the alloy was observed by scanning electron microscopy (SEM) and transmission electron microscopy (TEM), and the microstructural evolution, dislocation movement, and creep behavior of the alloy during creep were studied. The aim is to provide theoretical support for the engineering application of this alloy and the design of engine blades.

2. Experimental Materials and Methods

The material used in the experiment was the nickel-based single-crystal alloy IC9 (Ni-Al-Ti-Cr-Mo-W-Co). The alloy was made into a bar with an orientation of [111] by the seed crystal method. The deviation of the test bar from the [111] orientation was 10.4°, as determined by the Laue back reflection method. The heat treatment conditions were as follows: 1180°C/2 h + 1290°C/4 h, AC (air cooling) + 1000°C/4 h, and AC + 760°C/20 h. After complete heat treatment, the single-crystal bar was sheared into plate-like tensile creep samples along the (01$\bar{1}$) and ($\bar{2}$11) planes by wire cutting. The dimensions of the cross section were 4.5 mm × 2.5 mm, and the length of the gauge section was 15 mm. The axial direction of the applied stress was consistent with the solidification direction of the test bar. The creep properties of the alloy were tested at 1040°C/137 MPa, and the microstructural evolution, creep behavior, and fracture mechanism of the alloy were studied by SEM and TEM.

3. Experimental Results and Analysis

3.1. Microstructure of Alloys. The dendrite morphology in the solidification direction of the test bar is shown in Figure 1(a). Secondary dendrite morphology was an "X" type with angles of 60° or 120°, which had a regular arrangement and a relatively complex symmetric structure. The secondary dendrite arms in two directions were longer, and the secondary dendrite arms in the other two directions were shorter. Figure 1(b) shows the microstructural morphology of the end plane of the alloy test bar after complete heat treatment. The γ' phase was embedded in the γ phase, and it was in a triangular or hexagonal shape. Owing to the deviation of the orientation, the solidification end plane of the bar was not exactly the (111) plane, so the shapes of triangles or hexagons were irregular. Figure 1(c) shows the microstructure of the (01$\bar{1}$) plane after complete heat treatment. In the direction approximately 45° from the [111] orientation, the γ' phase was rectangular with a regular arrangement, and the γ' phase morphology of the ($\bar{2}$11) plane was similar to that of the (01$\bar{1}$) plane (figure omitted). The γ' phase was a regular rectangle arranged orderly along the [111] inclination direction. The microstructure of the alloy was still the cubic γ' phase, which was embedded in the γ phase in a coherent manner and regularly arranged along the <001> orientation. The stacking of the cubic γ' phase in space is shown in Figure 1(d).

3.2. Creep Characteristics of Alloys. The tensile creep test of the alloy at 1040°C/137 MPa showed that the creep life of the alloy was 352 h. The creep curve is shown in Figure 2, among

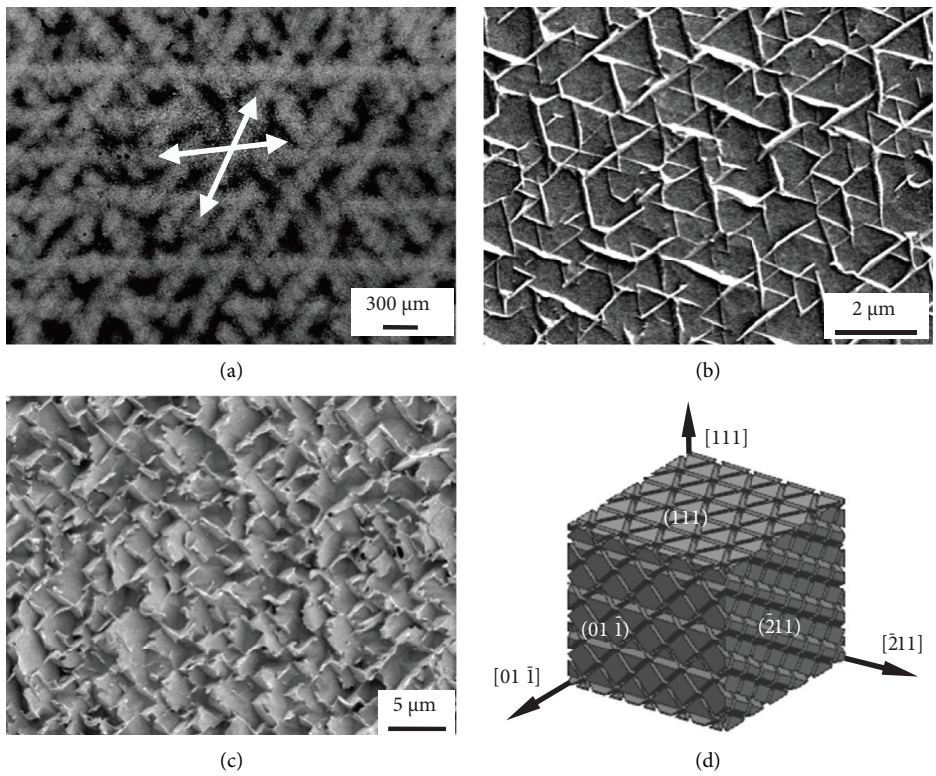

Figure 1: Dendritic morphology and microstructure of the γ' phase: (a) dendritic morphology of the (111) plane, (b) γ' phase morphology of the (111) plane, (c) γ' phase morphology of the (01$\bar{1}$) plane, and (d) stacking diagram of the γ' phase with the [111] orientation.

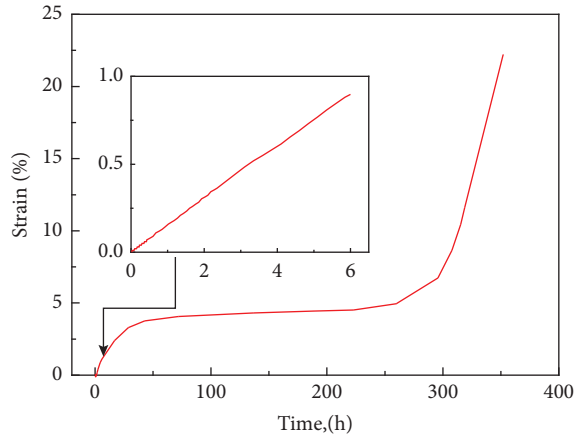

Figure 2: Creep curve of the alloy at 1040°C/137 MPa.

which the creep curve of the first 6 h is shown in the inset. The creep curve of the alloy showed a typical three-stage process. In the first stage of creep (deceleration creep stage), the creep rate decreased with time. After a short deceleration creep stage, the alloy rapidly entered the second creep stage (steady-state creep stage). During the steady-state creep stage, the creep rate of the alloy basically remained unchanged and lasted for a long period of time. The steady-state creep rate was about 0.0021%/h, and the duration of steady-state creep was about 300 h. After entering the third creep stage (accelerated creep stage), the strain rate and strain variable increased rapidly with time until fracture, and the total strain variable after 352 h of the creep fracture was 22.22%.

3.3. Deformation Characteristics of Alloys during Creep. The microstructures of the alloy after creep for 6 h, 50 h, and 352 h at 1040°C/137 MPa are shown in Figure 3. Figure 3(a) shows that after creep for 6 h, some of the matrix channels were cut off, cubic γ' phases were connected with each other, edges and corners were passivated, and the raft

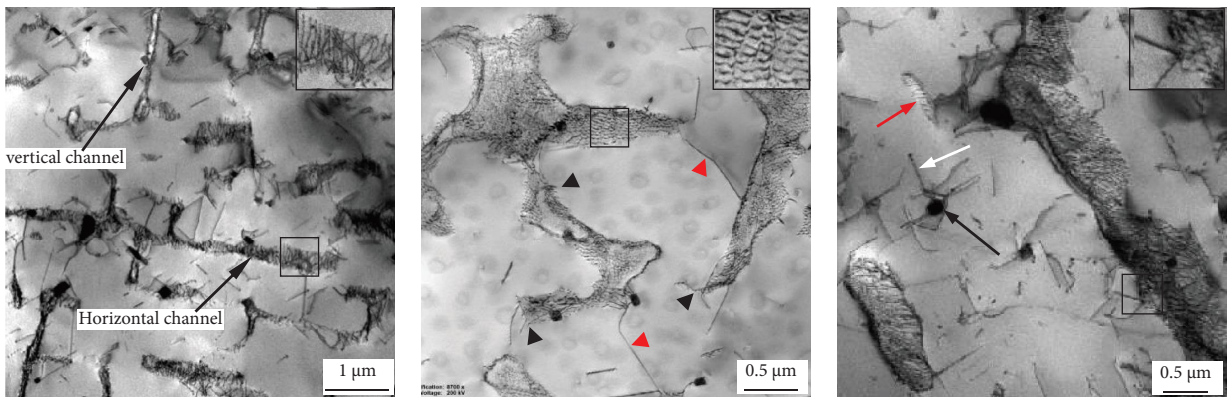

Figure 3: TEM images of the alloy creep different times at 1040°C/137 MPa: (a) 6 h, (b) 50 h, and (c) 352 h.

transformation of the γ' phases began. The figure shows that the width of the matrix channel in the horizontal direction was larger than that in the vertical direction, and the movement resistance of dislocations in the horizontal channel was smaller than that in the vertical channel. The primary dislocations in the matrix proliferated in the horizontal channel first, but the dislocation movement was limited in the γ phase, and many dislocations accumulated at the phase interface. The inset in the Figure 3(a) shows the magnified morphology of the dislocations in the box in the figure. Most of them were breeding dislocations in the same direction, which were typical primary dislocations in the first stage of creep. In addition, there were some dislocations in different directions, indicating that more than one slip systems were activated [17], and dislocations in different directions met and reacted to generate a dislocation network in the later creep process.

Figure 3(b) shows that after 50 h of creep, γ' phases diffused and connected to form a rafted structure, but the rafted structure of γ' phases was uneven in thickness and had discontinuous characteristics. Under the action of external and misfit stresses, the dislocations piled at the interface transformed into dislocation networks through dislocation reactions, but the shape of the dislocation network was irregular and the distribution was uneven, indicating that the creep of the alloy was uneven. The enlarged morphology of the dislocation network is shown in the inset in the figure which was a nearly quadrilateral dislocation network. Owing to the blocking of the dislocation network, there were few dislocations shearing into the γ' phase, and dislocations mainly crossed the γ' phase by climbing. The red triangles in the figure indicate dislocations that have climbed over the γ' phase, and the black triangles indicate dislocations that have not crossed the γ' phase at the beginning of climbing. The dislocation network could release the mismatch stress and restore the work hardening of the alloy. The dislocation network played a coordinating role in recovery softening caused by dislocation climbing and deformation hardening caused by dislocation accumulating in the γ phase, maintaining a dynamic balance between deformation hardening and recovery softening, thus improving the creep resistance of the alloy.

After 352 h of the creep fracture, as shown in Figure 3(c), the γ' and γ phases were coarsened, and the majority of dislocations sheared into the γ' phase, distorting the γ' phase and even causing crystal rotation, which resulted in misorientation with the adjacent γ' phase. Black contrast is evident in the figure, as indicated by the black arrow. In the later stages of creep, the dislocation network accumulated and formed dislocation entanglement at the γ/γ' interface, resulting in stress concentration and damaging the interface dislocation network. The dislocation cut into the γ' phase along the collapse of the dislocation network, as shown in the black box in the figure, and the enlarged morphology is shown in the inset in the figure. After the dislocation network was broken, it lost the hindering effect on the cutting of dislocations into the γ' phase, and creep accelerated until fracture. As shown in Figure 3(c), owing to the cutting of superdislocations, there were antiphase boundaries (APBs) in the γ' phase, as indicated by the white arrow. In addition, a superdislocation array was also found in the γ' phase, as shown by the red arrow in the figure. The superdislocation array was formed by the accumulation of dislocations continuously emitted by a dislocation source. The distance between two superpartials in the superdislocation was smaller, while the interval between superdislocations was larger.

Superdislocation arrays are rarely observed in the [001]-oriented and [011]-oriented samples. The Burgers vector of superdislocations was a <110> type in the superdislocation array, and the Schmid factor of the $<\bar{1}10>$-type superdislocation was 0 in the [111] orientation, which was a difficult slip-type superdislocation. The deviation of the orientation from the accurate [111] axis led to the formation of uneven deformation and irregular rafted structures, which caused the dislocations to accumulate near the irregular-rafted structure and produce stress concentration, providing a driving force for difficult slip superdislocations to shear into the γ' phase. The difficult slip superdislocations of the γ' phase could capture slip superdislocations, and dislocation reactions could occur to form a superdislocation network [18]. The immobility of difficult slip superdislocations and the capture behavior for slip superdislocations reduced the density of movable dislocations in the γ' phase, which was beneficial to the reduction of the creep rate and the creep

properties of the alloy [19]. When the number of superdislocations in the superdislocation array increased, stress concentration became larger. When it reached a certain level, the screw component of some superdislocations in the superdislocation array could cross slip over the obstacle. However, more often, microcracks initiated at the obstacle and caused damage. Under the continuous action of deformation, microcracks could grow beyond the critical size and cause macroscopic damage. Thus, the effect of the superdislocation array on the creep properties of the alloy was complicated.

3.4. Analysis of Dislocation Configuration after Creep Rupture. The dislocation morphology in the γ'phase after 352 h of the creep fracture at 1040°C/137 MPa is shown in Figure 4. There was a "V"-type superdislocation morphology, indicated by the letter A, an "X"-type superdislocation, indicated by the letter B, and other superdislocation morphologies, indicated by the letters C, D, E, and F.

The diffraction contrast analysis of the dislocation configurations A, B, C, and D in the γ' phase is shown in Figure 5. The "V"-type superdislocation morphology A contained three dislocations, labeled 1, 2 and 3, and the "X"-type superdislocation morphology B contained three dislocations, labeled I, II, and III. As shown in Figures 5(a) and 5(b), when the diffraction vector $g = [13\bar{1}]$ and [220], respectively, dislocations 1, 2, I, and II showed contrast. As shown in Figure 5(c), when $g = [1\bar{1}1]$, the contrast of dislocations 1, 2, and II disappeared and dislocation I showed contrast. As shown in Figure 5(d), when $g = [200]$, dislocations 1 and II showed contrast and the contrast of dislocations 2 and I disappeared. According to the dislocation invisibility criterion of g.b = 0, it was inferred that dislocations 1, 2, I, and II were superdislocations cutting into the γ' phase, and the Burgers vectors were $b_1 = [10\bar{1}]$, $b_2 = [011]$, $b_I = [01\bar{1}]$, and $b_{II} = [\bar{1}01]$, respectively. Dislocation 3 was generated by the reaction of dislocations 1 and 2, and the Burgers vector $b_3 = b_1 + b_2 = [110]$. Because superdislocations 1, 2, and 3 had double contrast, superdislocations 1, 2, and 3 could be decomposed into superpartial dislocations, and there were antiphase boundaries between superpartial dislocations. The trace direction of dislocation I was perpendicular to the diffraction vector $g = [220]$, and the trace direction of dislocation II was parallel to the diffraction vector $g = [220]$. According to $b \times \mu$, the slip plane of dislocation I was determined to be the (111) plane, and the slip plane of dislocation II was the $(1\bar{1}1)$ plane. Dislocation III was generated by the reaction of dislocations I and II, and the Burgers vector of dislocation III was $b_{III} = b_I + b_{II} = [\bar{1}10]$.

The formation process of the "V"-type superdislocation and the "X"-type superdislocation is shown in Figure 6. In Figure 6(a), b_1, b_2, and b_3 are the three slip directions on the $(1\bar{1}1)$ plane of the Thompson tetrahedron, the intersection angle between b_1 and b_2 was an obtuse angle, and two dislocations attracted each other. When superdislocations 1 and 2 met, they reacted to generate superdislocation 3, and the superdislocation could be decomposed to form

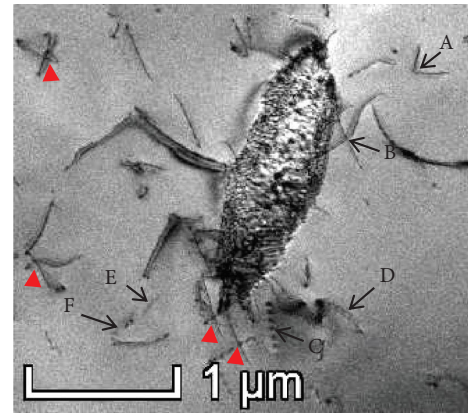

Figure 4: Dislocation morphology of the alloy after creep rupture at 1040°C/137 MPa.

superpartial dislocations and APBs, forming "V"-type superdislocation nodes. The distance between superpartial dislocations was the width of the APB, which was determined by the APB energy and repulsion between the same dislocations [20]. In Figure 6(b), the angle between dislocation I with the Burgers vector b_I in the (111) plane and dislocation II with the Burgers vector b_{II} in the $(1\bar{1}1)$ plane was an obtuse angle (120°), so dislocations I and II attracted each other. When dislocations I and II were close to each other, under the action of suction, the two dislocations converged and reacted to generate a new dislocation III with a Burgers vector b_{III}, forming a convergent dislocation configuration. If the two dislocations were to continue sliding, they would need to be separated from this convergence state, but if they were separated, work would need to be done to either form a cutting step or retract converging dislocations and achieve separation. Therefore, the formation of convergent dislocations increased the resistance of dislocation delivery, which had a hindering effect on deformation. Figure 4 shows that there were many similar convergent dislocation configurations, as indicated by the red triangle in the figure. Thus, the alloy had better creep resistance and longer creep life under this condition. In addition, the Schmid factor of the dislocation with the Burgers vector $<\bar{1}10>$ was 0 in the standard [111]-oriented sample. Owing to the existence of orientation deviation, although the $<\bar{1}10>$ dislocation in the experimental specimen had a smaller Schmid factor, the mobility was still poor, so the $<\bar{1}10>$-type dislocation also had a strengthening effect on the creep properties of the alloy.

When $g = [13\bar{1}]$, dislocations C and D showed weak contrast, as shown in Figure 5(a). When $g = [220]$, dislocation C showed weak contrast and dislocation D showed contrast, as shown in Figure 5(b). When $g = [1\bar{1}1]$, the contrast of dislocations C and D disappeared, as shown in Figure 5(c). When $g = [200]$, dislocation C showed contrast and dislocation D showed weak contrast, as shown in Figure 5(d). According to the dislocation invisibility criterion of g.b = 0, dislocations C and D showed double-line contrast. It was inferred that dislocations C and D were superdislocations with Burgers vectors $b_C = [\bar{1}01]$ and $b_D = [110]$, respectively. As shown in Figure 5(b), the trace

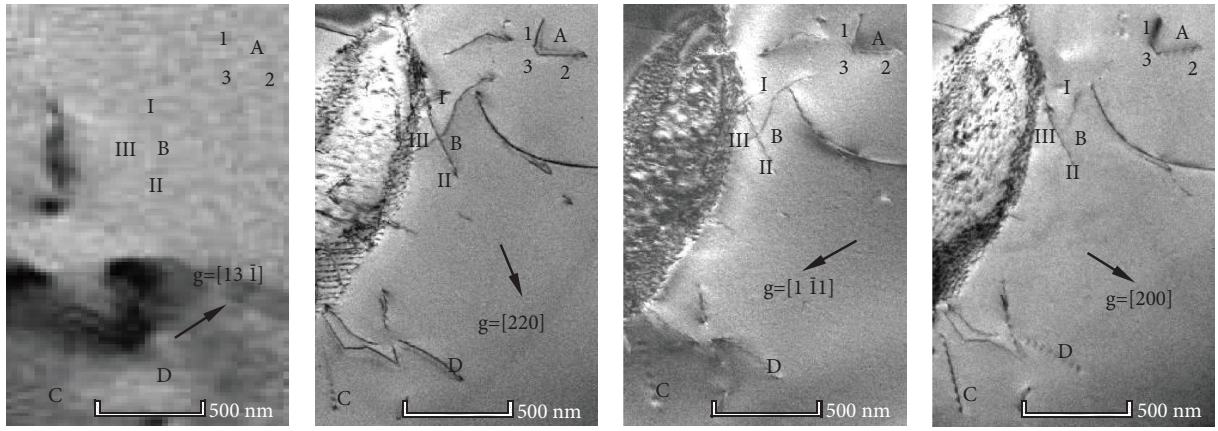

Figure 5: Dislocation configuration after the creep fracture at 1040°C/137 MPa: (a) g = [13̄1], (b) g = [220], (c) g = [1̄11], and (d) g = [200].

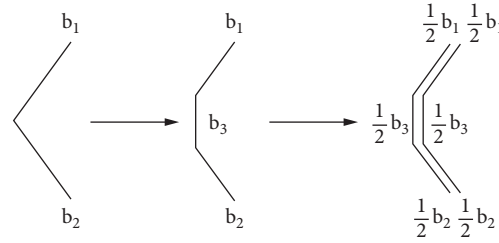

Figure 6: Continued.

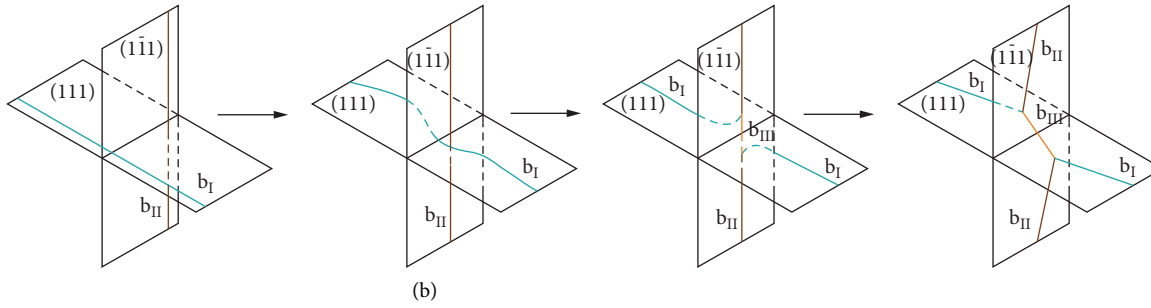

Figure 6: A schematic diagram of superdislocation formation: (a) formation of a "V"-type superdislocation node and (b) formation of an "X"-type convergent superdislocation.

direction of dislocation C was parallel to the diffraction vector g = [220]. According to $b_C \times \mu_C = (1\bar{1}1)$, the slip plane of dislocation C was the $(1\bar{1}1)$ plane. As shown in Figure 5(d), the trace direction of dislocation D was parallel to the diffraction vector g = [200], $b_D \times \mu_D = (001)$, and the slip plane of dislocation D was the (001) plane. Thus, the dislocation D was a K-W (Kear–Wilsdorf) lock formed by cross sliding from the {111} plane to the {100} plane. Furthermore, dislocations C and D had fringe characteristics, and the fringe direction was perpendicular to the direction of the dislocation trace, so there were antiphase boundaries between superpartial dislocations of C and D. Double-line contrast was obtained by the decomposition of superdislocations C and D via the process $b_C = 1/2[\bar{1}01] + \text{APB}_{(1\bar{1}1)} + 1/2a[\bar{1}01]$ and $b_D = 1/2[110] + \text{APB}_{(001)} + 1/2[110]$. The appearance of fringe contrast between superpartial dislocations was due to the large decomposition width and a certain angle of inclination to the observation plane [21].

The diffracted contrast analysis of dislocations E and F in Figure 4 after creep fracture at 1040°C/137 MPa is shown in Figure 7. When the diffraction vector g = [$\bar{2}$20] and g = [1̄11], the contrast of dislocation E disappeared and dislocation F showed weak contrast, as shown in Figures 7(a) and 7(b). When the diffraction vector g = [020], both dislocations E and F showed contrast, as shown in Figure 7(c). When diffraction vector g = [00$\bar{2}$], the contrast of dislocations E and F disappear, as shown in Figure 7(d). According to the dislocation invisibility criterion of g.b = 0

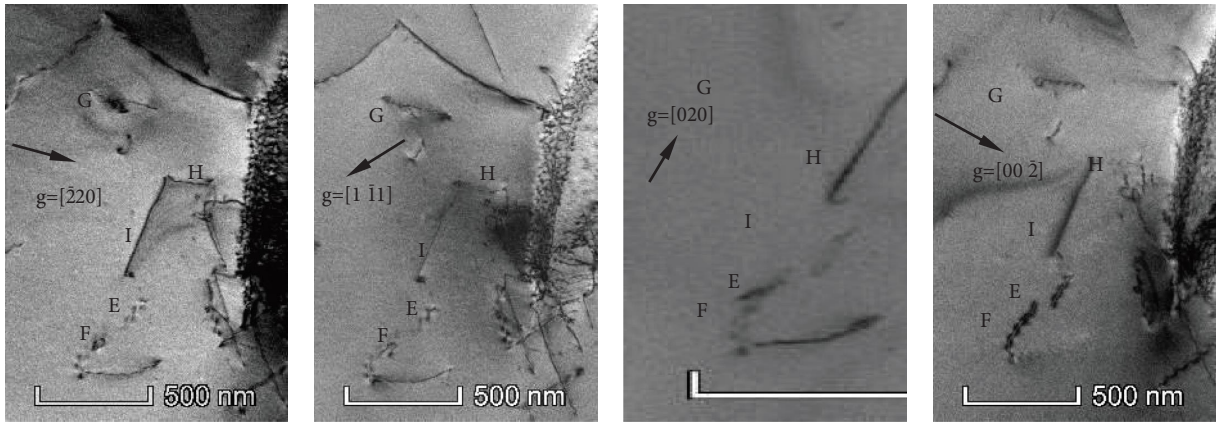

(a) (b) (c) (d)

Figure 7: Dislocation configuration after creep fracture at 1040°C/137 MPa: (a) g = [$\bar{1}$220], (b) g = [1$\bar{1}$11], (c) g = [020], and (d) g = [00$\bar{2}$].

and dislocations E and F showing double-line contrast, it was inferred that dislocations E and F were superdislocations of the Burgers vectors $b_E = [110]$ and $b_F = [1\bar{1}0]$, respectively. According to Figure 7(c), the trace direction of dislocations E and F was $\mu_E = \mu_F = [020]$, and since $b_E \times \mu_E = b_F \times \mu_F = (001)$, the slip plane of dislocations E and F was the (001) plane. According to the analysis, compared with the {100} plane, the {111} plane was the easy slip plane of the single-crystal alloy phase. Under the action of thermal activation during deformation, the activated <110> dislocations in the γ' phase could cross slide from the {111} plane to the {100} plane and decompose on the {100} plane to form the dislocation configuration of two 1/2<110> dislocations plus APBs [22]. Since the {100} plane was not the easy sliding plane of the γ' phase, the partial dislocations on the {100} plane were stationary dislocations, which pinned and hindered the continuous movement of dislocations on the {111} plane. Because dislocations E and F had fringe characteristics, the fringe direction was different from the direction of the dislocation trace. It was inferred that dislocations E and F were K-W locks formed by cross sliding from the {111} plane to the {100} plane, similar to dislocation D. The higher the temperature, the more easily the K-W locks formed due to thermal activation, which increased the critical shear stress of the dislocation sliding on the {111} plane. Therefore, the dislocation configuration could inhibit the dislocation slip and cross slip and ameliorate the deformation resistance of the alloy.

The diffraction analysis of the other dislocations (G, H, and I) in this region of the sample shown in Figure 7 is as follows: When the diffraction vector g = [020], the contrast of dislocation G disappeared and the rest showed contrast. Thus, $b_G = [101]$. Because the trace direction of dislocation G was parallel to g = [00$\bar{2}$], $b_G \times \mu_G = (010)$, and thus, the slip plane of dislocation G was the (010) plane. When g = [1$\bar{1}$1] and g = [020], the contrast of dislocation H disappeared, and thus, $b_H = [\bar{1}01]$. Because the trace direction of dislocation H was parallel to g = [$\bar{2}$20], $b_H \times \mu_H = (111)$, and thus, the slip plane of dislocation H was the (111) plane. When g = [1$\bar{1}$1], the contrast of dislocation I disappeared, and thus, $b_I = [011]$. Because the trace direction of dislocation I was parallel to g = [020], $b_I \times \mu_I = (100)$, and thus, the slip plane of dislocation I was the (100) plane. Therefore, dislocations G and I were K-W locks formed by the cross slip from the {111} plane to the {100} plane, similar to dislocations E and F, but the fringe characteristics of dislocations G and I were not evident, indicating that the decomposition width was small.

4. Discussion

4.1. Dislocation Movement and Creep Behavior of Alloys. The creep of nickel-based single-crystal superalloys starts from formation, movement, and evolution of dislocations in the matrix channel. In the high-temperature creep process of nickel-based single-crystal superalloys, dislocation movement runs through the whole creep process. The high-temperature creep behavior of the alloy can be explained by the dislocation movement mechanism during the creep process. At the first stage of creep at 1040°C/137 MPa, primary dislocations were first generated in the γ phase. The primary dislocations included misfit, slip, and extended dislocations. Of these, misfit dislocation existed before creep occurred, and the dislocation slip was the most basic deformation mechanism in the initial stage of creep. At the beginning of creep, the dislocation movement was confined within the γ phase. The dislocation accumulation in the γ phase led to deformation hardening, and the creep rate decreased. Under the action of external stress and misfit stress, dislocations in different slip systems were activated, dislocations in different directions met, and dislocation reactions occurred to form an interfacial dislocation network. The elastic coherent interface between the two phases transformed into a semicoherent interface, and the misfit stress was released. The interfacial dislocation network could prevent the γ phase dislocations from shearing into the γ' phase, promote the climbing of the dislocations over the γ' phase, and reduce stress concentration [23]. When deformation hardening caused by dislocation plugging and recovery softening caused by climbing reached the dynamic

equilibrium, the creep of the alloy entered the steady-state stage. The longer the dynamic equilibrium was maintained, the longer the creep life of the alloy was.

As creep progressed, when γ/γ' phase interfaces plugged too many dislocations and stress concentration could not be relieved by dislocation climbing, dislocation tangles formed at the interface and stress concentration occurred again. When the stress value at stress concentration was greater than the strength of the γ' phase, the interface dislocation network could be destroyed, the dislocations in the γ phase would be sheared into the γ' phase along the damage of the dislocation network, the dynamic equilibrium would be broken, and the alloy would enter the accelerated creep stage [23]. Under different strain rates or different temperatures, dislocation networks were reorganized and destroyed to varying degrees. When the strain rate was small, the dislocation network was partially destroyed, and only one dislocation around the dislocation node was destroyed. The deformation mechanism mainly manifested as a 1/2<110>-type dislocation cutting into the γ' phase. The cutting of the 1/2<110>-type dislocation destroyed the ordered structure of the γ' phase and caused energy changes. At this time, the 1/2<110>-type dislocation with the same Burgers vector restored the destroyed ordered structure, and there was a layer of APBs between front and rear dislocations. When the strain rate was large, most of the dislocation networks were destroyed, and dislocations around dislocation nodes were destroyed. Dislocations did not directly shear into the γ' phase, and voids formed at the interface. Dislocations piled up at the interface and sheared into the γ' phase in pairs to form superdislocations, such as superdislocations G, H, and I in Figure 7.

4.2. Theoretical Analysis of the Creep Resistance and Deformation Mechanism of Alloys. The microstructure of the nickel-based single-crystal alloy was such that the cubic γ' phase with a high volume fraction was embedded in the matrix in a coherent manner. The γ' phase was an intermetallic compound with an $L1_2$-type ordered structure, which could hinder the movement of dislocations during high-temperature creep, and it is an important strengthening phase of the alloy [24]. During the creep process, the dislocation motion was first confined to the matrix, the dislocation density in the matrix increased continuously, and stress concentration occurred at the γ/γ' phase interface. When the stress concentration value was greater than the yield strength of the γ' phase, the dislocation could be sheared into the γ' phase. Since the γ' phase was an important strengthening phase in the alloy, the dislocation of cutting could reduce the strength of the γ' phase and reduce the creep resistance of the alloy until creep rupture [25]. Therefore, the strength of the γ' phase was closely related to the creep resistance of the alloy [26]. According to the analysis, the strengthening methods of γ' phases mainly included solid solution strengthening, order strengthening, and γ/γ' phase coherent interface strengthening. At the first stage of creep, γ/γ' phases in the cubic state of the alloy maintained a coherent interface, and the lattice strain field could hinder dislocation shearing into the γ' phase. The resistance of the lattice strain field to delay the dislocation from cutting into the γ' phase can be expressed as follows:

$$\Delta\overrightarrow{\tau_1} = \beta.\mu.\varepsilon^{3/2}\left(\frac{r.f}{b}\right)^{1/2}, \quad (1)$$

where β is a constant related to the type of dislocation ($\beta = 3$ for edge dislocations and $\beta = 1$ for screw dislocations), μ is the shear modulus, ε is the lattice strain of the coherent interface, r is the radial dimension of the γ' phase, f is the volume fraction of the γ' phase, and b is the Burgers vector.

As creep progressed, γ' phases underwent rafting transformations, and there were a large number of dislocation networks at the interface. The sliding dislocation in the matrix could react with the dislocation network to change its original movement direction and climb to another sliding plane along the cutting step of the dislocation network under the action of thermal activation, which would slow stress concentration caused by dislocation stacking. The critical tensile stress σ required for the dislocation to climb over the γ' phase during the steady-state creep of the alloy at high temperatures/low stresses can be expressed as follows:

$$\sigma = \frac{\mu.b}{8\pi(1-\nu)\mathrm{h}}, \quad (2)$$

where ν is Poisson's ratio, and h is the height of dislocation climbing over the rafted γ' phase.

After the rafting transition, the γ/γ' phase interface changed from a coherent interface to a semicoherent interface, and the strengthening effect of the γ/γ' phase coherent interface was weakened. Therefore, in the later stage of creep, when high-density deformation dislocations in the γ phase caused stress concentration, the creep dislocations in the γ phase could shear into the phase due to the damage of the interface dislocation network. Since the γ' phase was an ordered structure, the perfect dislocation of the shear into the γ' phase was the <110> type. Compared with the 1/2<110>-type perfect dislocation in the γ phase, the displacement distance was doubled, so the dislocation shear into the γ' phase could cause large deformation.

For the nickel-based single-crystal alloy with the [111] orientation, the microstructure was still a cubic γ' phase embedded in the matrix in a coherent way and arranged regularly along the <100> orientation. If there was no orientation deviation in the [111]-oriented single-crystal alloy, when the tensile stress was applied along the [111] orientation of the single-crystal alloy, each crystal plane of the cubic γ' phase was symmetrically stressed, shear stress values were equal, and the strain energy density of each matrix channel and phase interface was symmetric and equal. Thus, the cubic γ' phase did not undergo raft transformation during creep. However, the alloy used in the experiment had an orientation deviation of 10.4°. Owing to the effect of the orientation deviation, the cubic γ/γ' phases of the alloy underwent asymmetric strain during high-temperature tensile creep, and the lattice of the cubic γ' phase of each crystal plane could undergo expansion or compression strain. The change in the strain energy density

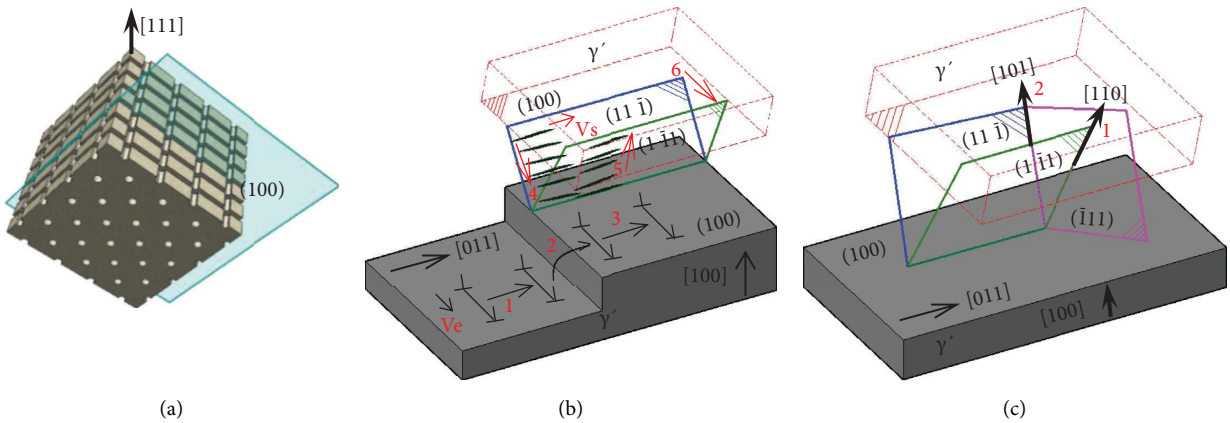

(a) (b) (c)

Figure 8: A schematic diagram of dislocation movement of the alloy during steady-state creep at 1040°C/137 MPa: (a) schematic diagram of γ' phase lamellar rafting, (b) slip, cross slip, and climbing of dislocations, and (c) obstruction of the γ' phase for the dislocation slip.

generated by different interfaces of the cubic γ' phase hexahedra acted as the driving force, which could promote the directional diffusion of elements and the directional growth of the γ' phase [27]. The crystal plane with a larger lattice expansion could trap Al, Ti, and other atoms with larger radii, which could promote the cubic γ' phase directional growth along the normal direction of the crystal plane and form raft structure morphology.

During the steady-state creep of the alloy at 1040°C/137 MPa, the γ' phase evolved into a two-dimensional lamellar-rafted structure parallel to the (100) plane. Of the three matrix channels parallel to the (100), (010), and (001) planes, the matrix channels parallel to the (010) and (001) planes were blocked, and only the matrix channel parallel to the (100) plane could be retained, as shown in Figure 8(a). Therefore, only the motion characteristics of dislocations in the matrix channel parallel to the (100) plane are analyzed here. Six slip systems could be activated during the high-temperature creep of the [111]-oriented alloy, which were ($\bar{1}$11) [101], ($\bar{1}$11) [110], (1$\bar{1}$1) [110], (1$\bar{1}$1) [011], (11$\bar{1}$) [101], and (11$\bar{1}$) [011]. The motion characteristics of dislocations in the matrix channel parallel to the (100) plane during steady-state creep are shown in Figures 8(b) and 8(c).

The motion characteristics of dislocations in the (1$\bar{1}$1) [011] and (11$\bar{1}$) [011] slip systems are shown in Figure 8(b). The edge dislocations with a trace direction V_e could smoothly slip along the [011] direction in the matrix channel parallel to the (100) plane, as shown by arrows 1 and 3 in the figure. When the slip dislocation was hindered by the γ' phase and the shear stress component acting on the dislocation was large enough, the dislocation crossed the γ' phase by climbing, as shown by arrow 2 in the figure. The screw dislocation with a trace direction V_s could slip on the (11$\bar{1}$) plane, as shown by arrow 4. When the dislocation moved to the γ' phase and was blocked by the γ' phase, it could cross slip to the (1$\bar{1}$1) plane, as shown by arrow 5. This process was equivalent to the screw dislocation sliding on the (100) plane, as shown by arrow 6, which could cause the screw dislocation to pass through the narrow matrix channel [28]. Since the dislocations in the (1$\bar{1}$1) [011] and (11$\bar{1}$) [011] slip systems had the same Burgers vectors, it only resulted in a weaker strain hardening effect.

In addition, the motion characteristics of the dislocations in the other four mobile slip systems in the [111]-oriented alloy are shown in Figure 8(c). The movement of dislocations in the matrix was hindered by the lamellar γ' phase, as shown by arrows 1 and 2 in the figure. Therefore, compared with the slip and cross slip of dislocations in the matrix channel (Figure 8(b)), the resistance of dislocation movement in these four slip systems was larger. So, during the steady-state creep of the [111]-oriented alloy at 1040°C/137 MPa, the dislocation slip and cross slip in the matrix channel parallel to the (100) plane were the main deformation mechanisms of the alloy.

5. Conclusion

(1) During creep at 1040°C/137 MPa, the orientation deviation of the alloy led to the asymmetry of the stress and unequal values of the shear stress in each crystal plane of the γ' phase, which promoted the directional diffusion of elements and the directional growth of the γ' phase. The γ' phase transformed into a two-dimensional lamellar raft structure parallel to the (100) plane, blocking the matrix channel parallel to the (010) and (001) planes.

(2) During steady-state creep, the interfacial dislocation network and the strengthening effect of the γ' phase itself effectively hindered the matrix dislocations from shearing into the γ' phase. So the alloy had good deformation resistance. The slip and cross slip of dislocations in the matrix channel parallel to the (100) plane were the main deformation mechanisms during steady-state creep

(3) In the accelerated creep stage, the dislocation network was destroyed. The dislocations sheared into the γ' phase via dislocation pairs, which could react to form superdislocation nodes and decompose to form APBs on the <111> surface or cross slip from the <111> plane to the <100> plane to form K-W locks.

Data Availability

No data were used to support this study.

Conflicts of Interest

The authors declare that they have no conflicts of interest.

Acknowledgments

This work was supported by the Youth Science and Technology Talents Growth Project of Guizhou Province (qianjiaoheKYzi[2020]145, qianjiaoheKYzi[2022]121), the Characteristic Key Laboratory of University of Guizhou Province (qianjiaoheKYzi[2019]053), and the Science and Technology Foundation Project of Guizhou Province (qiankehezhicheng [2019] 2870, qiankehezhicheng [2019] 2843).

References

[1] Z. Hou and T. Lei, "Constrained model free adaptive predictive perimeter control and route guidance for multi-region urban traffic systems," *IEEE Transactions on Intelligent Transportation Systems*, vol. 23, no. 2, pp. 912–924, 2022.

[2] Y. Zhang, W. Guo, and Q. Yan, "Composition, microstructure and mechanical homogeneity evaluation of the Y-bearing 9Cr F/M steel fabricated by VIM & casting technique," *Materials Research Express*, vol. 7, no. 3, Article ID 036518, 2020.

[3] L. Liu, T. W. Huang, J. Zhang, and H. Z. Fu, "Microstructure and stress rupture properties of single crystal superalloy CMSX-2 under high thermal gradient directional solidification," *Materials Letters*, vol. 61, no. 1, pp. 227–230, 2007.

[4] Z. Lou, Y. Yan, Y. Geng, X. Zhao, and Z. Hao, "The effect of anisotropy of nickel-based single crystal alloys on the surface quality of sub-nanometer and near atomic scale cutting," *Intermetallics*, vol. 145, Article ID 107536, 2022.

[5] R. A. Mackay and R. D. Maier, "The influence of orientation on the stress rupture properties of nickel-base superalloy single crystals," *Metallurgical Transactions A*, vol. 13, no. 10, pp. 1747–1754, 1982.

[6] G. R. Leverant and B. H. Kear, "The mechanism of creep in gamma prime precipitation-hardened nickel-base alloys at intermediate temperatures," *Metallurgical and Materials Transactions B*, vol. 1, no. 2, pp. 491–498, 1970.

[7] J. Yu, J. R. Li, J. Q. Zhao et al., "Orientation dependence of creep properties and deformation mechanism in DD6 single crystal superalloy at 760°C and 785MPacreep properties and deformation mechanism in DD6 single crystal superalloy at 760°C and 785MPa," *Materials Science and Engineering: A*, vol. 560, pp. 47–53, 2013.

[8] C. M. F. Rae, N. Matan, and R. C. Reed, "The role of stacking fault shear in the primary creep of [001]-oriented single crystal superalloys at 750 °C and 750 MPa," *Materials Science and Engineering: A*, vol. 300, no. 1-2, pp. 125–134, 2001.

[9] C. M. F. Rae, M. A. Rist, D. C. Cox, R. C. Reed, and N. Matan, "On the primary creep of CMSX-4 superalloy single crystals," *Metallurgical and Materials Transactions A*, vol. 31, no. 9, pp. 2219–2228, 2000.

[10] C. M. F. Rae and R. C. Reed, "Primary creep in single crystal superalloys: origins, mechanisms and effects," *Acta Materialia*, vol. 55, no. 3, pp. 1067–1081, 2007.

[11] H. Fu, S. S. Li, Y. L. Pei, and S. K. Gong, "Effect of Al content on microstructure and creep behavior of low density Ni₃Al-base single crystal superalloy," *Materials Science Forum*, vol. 816, pp. 297–303, 2015.

[12] M. Hantcherli, F. Pettinari-Sturmel, B. Viguier, J. Douin, and A. Coujou, "Evolution of interfacial dislocation network during anisothermal high-temperature creep of a nickel-based superalloy," *Scripta Materialia*, vol. 66, no. 3-4, pp. 143–146, 2012.

[13] V. Sass, U. Glatzel, and M. Feller-Kniepmeier, "Anisotropic creep properties of the nickel-base superalloy CMSX-4," *Acta Materialia*, vol. 44, no. 5, pp. 1967–1977, 1996.

[14] X. Wu, J. H. Zhang, J. L. Liu, T. Jin, Y. B. Xu, and Z. Q. Hu, "Plastic deformation inhomogeneity in a single crystal nickel-base superalloy," *Materials Science and Engineering: A*, vol. 325, no. 1-2, pp. 478–483, 2002.

[15] J. Yu, J. R. Li, S. Z. Liu, and M. Han, "Creep anisotropy in single-crystal superalloy DD6 near the [001] orientation," *Superalloys 2020*, vol. 29, pp. 303–311, 2020.

[16] D. P. Pope and S. S. Ezz, "Mechanical properties of Ni_3AI and nickel-base alloys with high volume fraction of γ," *International Materials Reviews*, vol. 29, no. 1, pp. 136–167, 1984.

[17] G. L. Wang, J. L. Liu, J. D. Liu et al., "Temperature dependence of tensile behavior and deformation microstructure of a Re-containing Ni-base single crystal superalloy," *Materials & Design*, vol. 130, pp. 131–139, 2017.

[18] Y. F. Li, L. Wang, G. Zhang et al., "Creep deformation related to γ' phase cutting at high temperature of a [111] oriented nickel-base single crystal superalloy," *Materials Science and Engineering: A*, vol. 763, Article ID 138162, 2019.

[19] P. Wang, W. Hao, J. Xie, J. Ding, F. Wang, and C. Huo, "Primary creep X80 pipeline steel at room temperature using molecular dynamics simulationcreep X80 pipeline steel at room temperature using molecular dynamics simulation," *Applied Physics A*, vol. 128, no. 3, p. 204, 2022.

[20] K. Yashiro, F. Kurose, Y. Nakashima, K. Kubo, Y. Tomita, and H Zbib, "Discrete dislocation dynamics simulation of cutting of γ' precipitate and interfacial dislocation network in Ni-based superalloys," *International Journal of Plasticity*, vol. 22, no. 4, pp. 713–723, 2006.

[21] T. Ning, T. Sugui, Y. Huajin, S. Delong, Z. Shunke, and Z. Guoqi, "Deformation mechanisms and analysis of A single crystal nickel-based superalloy during tensile at room temperature," *Materials Science and Engineering: A*, vol. 744, pp. 154–162, 2019.

[22] G. Zhao, S. Tian, S. Zhang, N. Tian, and L. Liu, "Deformation and damage features of a Re/Ru-containing single crystal nickel base superalloy during creep at elevated temperature," *Progress in Natural Science: Materials International*, vol. 29, no. 2, pp. 210–216, 2019.

[23] G. Wang, S. Zhang, S. Tian, N. Tian, G. Zhao, and H. Yan, "Microstructure evolution and deformation mechanism of a [111]-oriented nickel-based single-crystal superalloy during high- temperature creep," *Journal of Materials Research and Technology*, vol. 16, pp. 495–504, 2022.

[24] H. J. Yan, Su G. Tian, G. Qi Zhao, and S. Ke Zhang, "Deformation features of a high Mo nickel-based single crystal superalloy during creep at high temperature," *Key Engineering Materials*, vol. 795, pp. 35–42, 2019.

[25] X. Zhou, X. Pan, and F. Berto, *A State of the art Review on Creep Damage Mechanics of Rocks*, Fatigue & Fracture of Engineering Materials & Structures, 2022.

[26] J. Xie, S. Tian, L. J. Shang, and X. Zhou, "Creep behaviors and role of dislocation network in a powder metallurgy Ni-based

superalloy during medium- temperature," *Materials Science and Engineering A*, vol. 606, pp. 304–312, 2014.

[27] C. Y. Cui, A. Sato, Y. F. Gu, D. H. Ping, H. Harada, and A. Sato, "Phase stability and yield stress of Ni-base superalloys containing high Co and Ti," *Metallurgical and Materials Transactions A*, vol. 37, no. 11, pp. 3183–3190, 2006.

[28] V. Sass and M. Feller-Kniepmeier, "Orientation dependence of dislocation structures and deformation mechanisms in creep deformed CMSX-4 single crystals," *Materials Science and Engineering A*, vol. 245, no. 1, pp. 19–28, 1998.